Journal of
Synchrotron
Radiation

ISSN 0909-0495

Received 20 November 2009
Accepted 3 February 2010

Tracing X-rays through an L-shaped laterally graded multilayer mirror: a synchrotron application

Marcelo Goncalves Honnicke,* Xianrong Huang, Jeffrey W. Keister, Chaminda Nalaka Kodituwakku and Yong Q. Cai

National Synchrotron Light Source II, Brookhaven National Laboratory, Brookhaven, NY 11973-5000, USA. E-mail: mhonnicke@bnl.gov

A theoretical model to trace X-rays through an L-shaped (nested or Montel Kirkpatrick–Baez mirrors) laterally graded multilayer mirror to be used in a synchrotron application is presented. The model includes source parameters (size and divergence), mirror figure (parabolic and elliptic), multilayer parameters (reflectivity, which depends on layer material, thickness and number of layers) and figure errors (slope error, roughness, layer thickness fluctuation $\Delta d/d$ and imperfection in the corners). The model was implemented through *MATLAB/OCTAVE* scripts, and was employed to study the performance of a multilayer mirror designed for the analyzer system of an ultrahigh-resolution inelastic X-ray scattering spectrometer at National Synchrotron Light Source II. The results are presented and discussed.

© 2010 International Union of Crystallography
Printed in Singapore – all rights reserved

Keywords: X-ray optics; X-ray mirrors; ray tracing; multilayer simulation; high resolution.

1. Introduction

In X-ray optics, elements such as reflective mirrors operate in total reflection within a small critical angle (θ_c), beyond which the reflectivity drops rapidly to zero. This is due to the fact that the real part (δ) of the refraction index ($n = 1 - \delta + i\beta$) in the hard X-ray spectral range is extremely small ($\sim 10^{-6}$). Reflective mirrors are widely used in synchrotron X-ray beamlines as collimating and focusing optics. Also, they can be used as the first optical element to reduce the heat load impinging on the monochromator and as a harmonic suppressor. With the advent of new polishing techniques (Jain, 2008), such as abrasive flow machining (Rhoades, 1991) and magnetorheological finishing (Kordonski & Jacobs, 1996), and with the improvement of sputtering deposition systems, the use of mirrors and challenging mirror surfaces [*e.g.* Wolter mirrors for soft X-ray microscopy (Sugisaki *et al.*, 1998)] has become more popular. However, manufacturing high-quality mirrors for hard X-ray energies is still a major challenge. At higher energies the critical angle becomes much smaller ($\theta_c = \delta^{1/2}$), which requires, in general, a longer mirror and a surface of higher accuracy in order to reduce angular spread caused by slope error. Also shorter photon wavelength requires smaller values of roughness in order to reduce the intensity loss owing to diffuse scattering.

One way to circumvent this problem is to use diffractive multilayer mirrors. Using these the angle of incidence can be increased and therefore the slope errors can be relaxed. In the X-ray spectral range, multilayer mirrors were first successfully fabricated in the early 1940s as superlattices using the evaporation techniques (Dumond & Youtz, 1940). The multilayer is an artificial structure composed of layers of alternating soft and heavy materials, thereby creating an artificial lattice. Such structures become much more useful (Vinogradov & Zeldovich, 1977; Lienert *et al.*, 1999; Champeaux *et al.*, 2007) with the advent of new sputtering deposition techniques that make it possible to control the layer thickness with a precision better than 0.2 nm (Schuster & Gobel, 1995). This makes it possible to build laterally graded multilayers, *i.e.* structures with the lattice parameter (the d spacing) varying for different points on the mirror surface, in order to improve the efficiency of the diffractive optics. The advantage of such a structure is that higher intensity at higher reflection angles can be obtained owing to diffraction by the artificial lattice. Laterally graded multilayer mirrors, for example, have been used to increase the bandwidth (to $\Delta\lambda/\lambda \simeq 10^{-3}$) of beamline monochromators. Their use as collimators (Goebel mirrors) in conventional X-ray sources, to improve the intensity in powder diffraction experiments, has also been reported (Hertlein *et al.*, 2005; Shymanovich *et al.*, 2008).

In many cases the application of multilayer mirrors involves only one-dimensional figuring owing to the challenge in fabricating a mirror with an aspherical surface figure. L-shaped laterally graded multilayer mirrors provide a solution to this problem by combining two one-dimensionally figured multilayer mirrors at 90° to each other. Such types of mirror have been used in commercial powder diffratometers (Hertlein *et al.*, 2005; Shymanovich *et al.*, 2008) and also with neutron sources (Ice *et al.*, 2009). By having two diffractions at each surface (Fig. 1), these mirrors can be used to focus (elliptic figure) or collimate (parabolic figure) the beam into

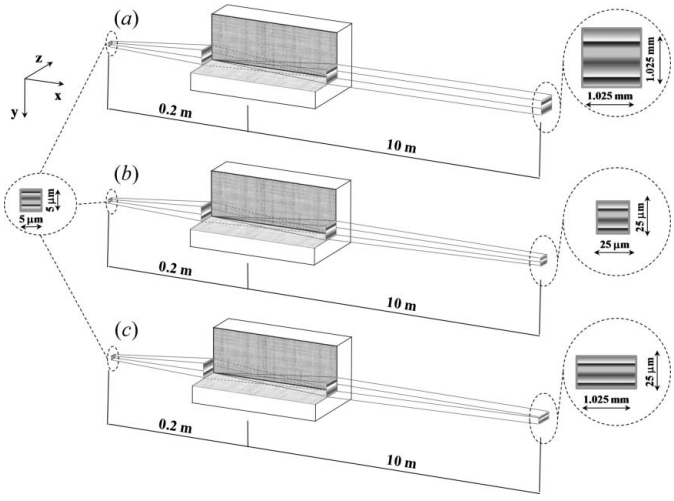

Figure 1
Schematic representation of the L-shaped double-bounce X-ray mirror used as (*a*) collimator (parabolic figure), (*b*) focusing optic (elliptic figure) and (*c*) focusing/collimating optic (combination of parabolic and elliptic figure). The insets show the theoretical focus sizes for perfect mirrors.

two dimensions. They can also be used to focus the beam into one direction and collimate in another (with a vertical elliptic mirror and a horizontal parabolic mirror or *vice versa*). The disadvantage of having two diffractions, compared with an aspherical surface, is compensated by the possibility to carry out more accurate surface figuring. Compared with the Kirkpatrick–Baez geometry (Kirkpatrick & Baez, 1948), L-shaped laterally graded multilayer mirrors present the advantage of having the same focus distance for the vertical and horizontal mirror.

To simulate such a multilayer mirror, one can use some excellent ray-tracing programs dedicated to X-rays (freely available) which include *SHADOW* (Lai & Cerrina, 1986) and *RAY* (Schafers, 2008). Also, other programs such as *ZEMAX*, *Tracepro* and *Code V*, which handle visible-light optics, are commercially available. The reason for having dedicated ray-tracing programs for X-rays is because such programs consider two important main issues: X-ray refraction index (smaller than 1) and dynamical diffraction effects (Authier, 2001). Among the dedicated X-ray ray-tracing programs, *SHADOW* does not handle laterally graded multilayers, whereas *RAY* does. However, both are not able to easily trace X-rays into L-shaped mirrors. In this manuscript we present a theoretical model to trace X-rays through L-shaped laterally graded multilayer mirrors. The model was implemented in *MATLAB/OCTAVE* scripts. The input parameters used here are those required for the analyzer system of the high-resolution inelastic X-ray scattering (IXS) spectrometer at NSLS II. In the IXS spectrometer the L-shaped laterally graded multilayer mirror needs to accept the scattering of the sample with an aperture of 5 mrad and collimate this beam to 0.1 mrad. This collimation has to be the acceptance of a high energy resolution analyzer crystal system (Shvyd'ko *et al.*, 2006; Yabashi *et al.*, 2001; Toellner *et al.*, 1997) in order to improve the efficiency of the spectrometer. Other options like separated Kirkpatrick–Baez multilayer mirror systems and aspherical multilayers could also do the job.

Different mirror figures were exploited: parabolic and elliptic and a combination of both (Fig. 1). These mirror figures work in different configurations: collimator, focusing and combination of vertical focusing and horizontal collimation. The beam being diffracted by the mirror is characterized in terms of source parameters (source size and divergence), figure errors (slope error, roughness and the random layer thickness fluctuation $\Delta d/d$) and corner gap.

2. Theoretical model

The first step to tracing X-rays through a multilayer mirror is to set up the odd and even multilayer materials and also the number of bi-layers in the multilayer structure. These parameters will determine the efficiency of the multilayer mirror. The next step is to calculate the reflectivity. To do this the dynamical theory of X-ray diffraction for angles near grazing incidence needs to be applied (Authier, 2001; Parrat, 1954; Underwood & Barbee Jr, 1981). By using the formalism developed by Parrat (1954) and improved by Underwood & Barbee Jr (1981) one can plot the reflectivity curve shown in Fig. 2 (solid line) for a flat multilayer mirror. The curve was calculated with parameters optimized for maximum reflectivity: W/B_4C multilayer mirror for 100 bi-layers (2.5 nm each, W 1.0 nm thick and B_4C 1.5 nm thick). This curve shows an asymmetry and some oscillations around the main peak. Both effects are a consequence of the dynamical theory of X-ray diffraction. The asymmetry is due to the different photoelectric absorption of the standing X-ray wavefield (Honnicke & Cusatis, 2009) for the low- and high-angle side of the

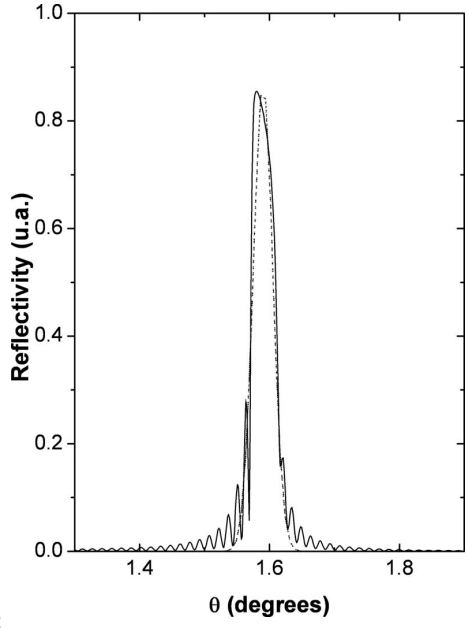

Figure 2
Theoretical reflectivity for a W/B_4C flat multilayer mirror for a total of 100 bi-layers (2.5 nm each, W 1.0 nm thick and B_4C 1.5 nm thick) (solid curve) and the approximation, as a Gaussian profile, used in the simulations (dotted curve).

rocking curve. The oscillations are the Pendellösung fringes owing to the finite crystal condition. If the multilayer was thicker, these oscillations would disappear. In our model the reflectivity is approximated by a Gaussian profile (Fig. 2, dotted line) with the same amplitude and full width at half-maximum (FWHM) of the theoretical reflectivity curve (w = 5.2×10^{-4} rad). So, different types of multilayer (layer materials, lattice parameter and number of bi-layers) can be used as input to account for the reflectivity in the scripts.

Once the materials to be used for the multilayer have been established, other parameters for ray tracing the X-ray through the mirror must be determined. These include source parameters (size and divergence), figure errors (slope error, roughness and random layer thickness fluctuation) and corner gap. These parameters are specified in the following sections and used as input for the ray-tracing program.

2.1. Mirror figure

In the present theoretical model we are using parabolic and elliptic figures and a combination of both, as shown in Fig. 1. For the parabolic figure the required parameter is the focal parameter (p) and is given by the parabolic equations

$$y = (2px)^{1/2}, \qquad z = (2px)^{1/2}. \tag{1}$$

The input parameters to determine p are the source-to-mirror distance (s) and the incident angle (θ_i). The relation between p, s and θ_i can be easily found by simple trigonometric calculations and is given by

$$\theta_i = \operatorname{arccot}\left[(2s/p - 1)^{1/2}\right]. \tag{2}$$

Another useful relation is how p is related to the focus distance, F,

$$p = 2F. \tag{3}$$

The parameters s, θ_i and F ($F = p/2$) are schematically shown in Fig. 3(a). A parabolic mirror figure for s = 200 mm and $\theta_i = 1.59^\circ$ (p = 0.308 mm) is shown in Fig. 4(a).

For the elliptic figure, the required parameters are a and b, as given by the elliptic equation

$$\begin{aligned} y &= b\left(1 - x^2/a^2\right)^{1/2}, \\ z &= b\left(1 - x^2/a^2\right)^{1/2}. \end{aligned} \tag{4}$$

The equations (1)–(4) are for only the cases of a plane ellipse and a plane parabola. The input parameters to the program to determine a and b are the source-to-mirror distance (s_1), the mirror-to-focus distance (s_2) and the incident angle (θ_i). To determine a, the following relation can be used,

$$a = (s_1 + s_2)/2. \tag{5}$$

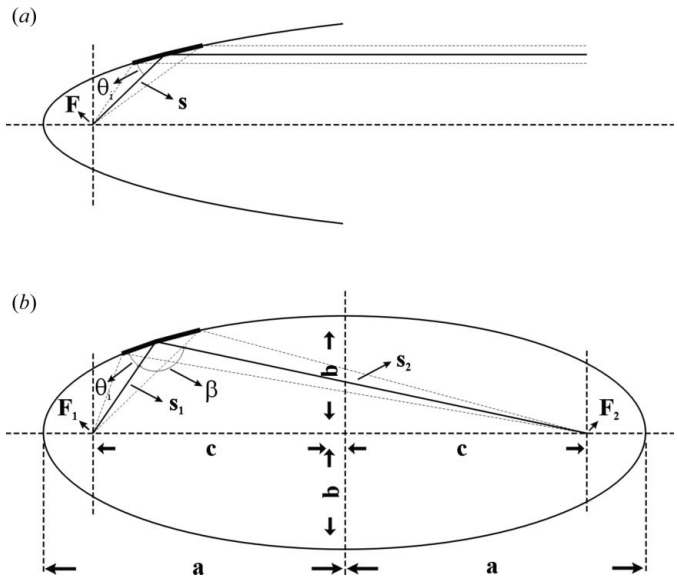

Figure 3
Schematic representation of the main figure parameters: (a) parabolic figure and (b) elliptic figure.

To determine b, we first need to specify β (the angle between s_1 and s_2),

$$\beta = \pi - 2\theta_i; \tag{6}$$

by the law of cosines,

$$(2c)^2 = s_1^2 + s_2^2 - 2s_1 s_2 \cos(\beta), \tag{7}$$

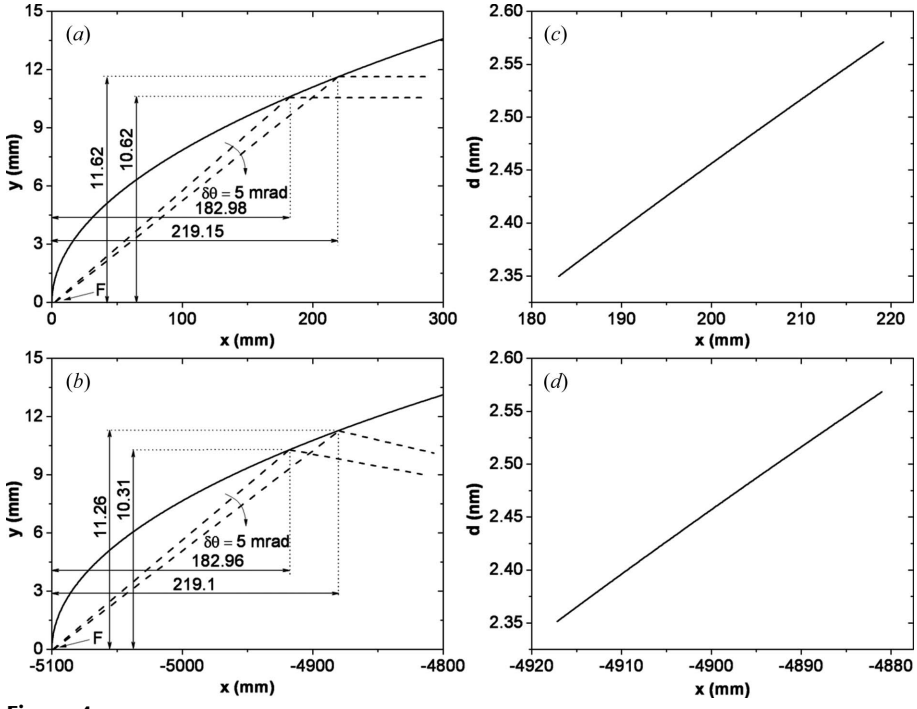

Figure 4
Mirror figures and parameters used as input in the ray-tracing program: (a) parabolic, (b) elliptic, (c) variation in the lattice parameter *versus* distance on the mirror surface for the parabolic laterally graded multilayer, (d) variation in the lattice parameter *versus* distance on the mirror surface for the elliptic laterally graded multilayer mirror. Different inputs for parabolic and elliptic surfaces can also be used in the program.

where $2c$ is the distance between the two foci (F_1 and F_2). With c we can determine the eccentricity (ε) by

$$c = \varepsilon a. \tag{8}$$

So b can be found by

$$b = \left(1 - \varepsilon^2\right)^{1/2} a. \tag{9}$$

The parameters a, b, s_1, s_2, θ_i, β, c, F_1 and F_2 are schematically shown in Fig. 3(b). An elliptic mirror figure for s_1 = 200 mm, s_2 = 10000 mm and $\theta_i = 1.59^\circ$ is shown in Fig. 4(b). The abscissa scales in Fig. 4(a) and 4(b) are different so as to be mathematically consistent with the equations shown above.

2.2. Source parameters

The source parameters as the input for the ray-tracing program are the source size (σ, defined by the FWHM) and the divergence ($\Delta\theta$, the full angle). If the source size is infinitely small (point source), the size of the beam (ω, defined by the FWHM) after a perfect mirror (for the parabolic figure) can be predicted by the simple geometric relation

$$\omega = \Delta\theta s. \tag{10}$$

For a point source and the elliptic figure mirror, the size of the beam on the focus (s_2) will be the same as in source (s_1), *i.e.* a point. When a finite source is included, these parameters are changed. They can also be predicted by geometric relations. The sizes of the beam (ω) after the mirror, for parabolic and elliptic figures, are given by equations (11) and (12), respectively,

$$\omega \simeq \frac{\sigma}{\cos\theta_i} + \Delta\theta f, \tag{11}$$

$$\omega \simeq \sigma(f_2/f_1) + \Delta\theta f_1. \tag{12}$$

In the present simulations both cases can be considered (point source or extended source). The trace of the X-rays is made for each ray (250000 in total) that reaches the mirror surface at different angles of incidence (aberrations owing to the incorrect incident angle owing to the source size are considered). This procedure is helpful when the surface errors are included, as each ray will be touching a different point on the surface.

2.3. Slope error

The slope error, or waviness, is almost always considered as short-range sinusoidal-like variations from the ideal surface shape. If this kind of variation is of over a large range it is called the figure error. The slope error is responsible for the image spread on the focal plane and also for a reduction of the intensity owing to the shadowing effect of the ripples (Sanchez Del Rio & Marcelli, 1992).

The slope error introduced in the present model is considered to be sinusoidal-like in the direction of the beam (meridional slope error) on both surfaces. When the input parameter is the slope error, the probe for the entire sinusoidal function (ripple wavelength) is chosen to be

$$S \simeq A\sin(2\pi/\Lambda), \tag{13}$$

where A is the ripple amplitude and Λ is the wavelength of the sinusoidal slope error. Based on this function, the slope error number is given by the derivative of this function with respect to Λ, point by point on the mirror surface.

2.4. Roughness

In general, roughness is defined by the inhomogeneity of the surface. Its size is considered to be of the order of the wavelength (a few tenths of a nanometer for X-rays), and thus it produces diffuse scattering (Debye *et al.*, 1957; Wong, 1985; Sinha *et al.*, 1988; Kopecky, 1994; Bruson, 1995; Stepanov *et al.*, 1996; Vainer *et al.*, 2006). Usually, roughness is considered by defining a correlation function. The correlation function gives the extension of the inhomogeneity, *i.e.* the size of the region over which they occur. When the Born approximation is used, the scattered function is proportional to the Fourier transformation of the correlation function. The correlation function used here is based on a scattering model involving a homogeneous surface with several holes of random size (Debye *et al.*, 1957). This gives us a correlation function for a random scatter given by

$$\gamma(r) \simeq \exp(r/a), \tag{14}$$

where a is given by the extension of the inhomogeneity and it is, usually, of the order of ten thousandths of a nanometer. A similar approach can be made by using the formalism proposed by Sinha *et al.* (1988) with h, in his nomenclature, equal to 0.5. Following the mathematics given by Debye *et al.* (1957), the scattered intensity is given by

$$i = \frac{8\pi a^3 \langle \eta^2 \rangle V}{\left(1 + k^2\theta^2 a^2\right)^2}, \tag{15}$$

where a has been defined above, η is the local fluctuation from an average electron density (proportional to the RMS roughness σ, that is the input in the ray-tracing program), V is the illuminated volume, $k = 2\pi/\lambda$ and θ is the scattering angle. The reflectivity intensity including the scattering is shown as a dotted Gaussian profile in Fig. 5. Such a curve is used as a reflectivity curve when roughness is included. Different values for the roughness can be used as input.

2.5. Random layer thickness fluctuation

This kind of imperfection is characterized by the random variation in the layer thickness around its nominal value at that spatial position on the mirror. It is treated here as the relative variation in the lattice parameter ($\Delta d/d$); this is the input in the ray-tracing program. When this is included, the reflectivity (Gaussian profile) becomes broadened (Fig. 5). The area of the Gaussian profile is kept constant, so that the peak intensity is reduced owing to the variation in the lattice parameter.

2.6. Mirror corner

One of the important points raised by the synchrotron community concerns the corner of the L-shaped mirrors. The corner is an important issue which arises when assembling the

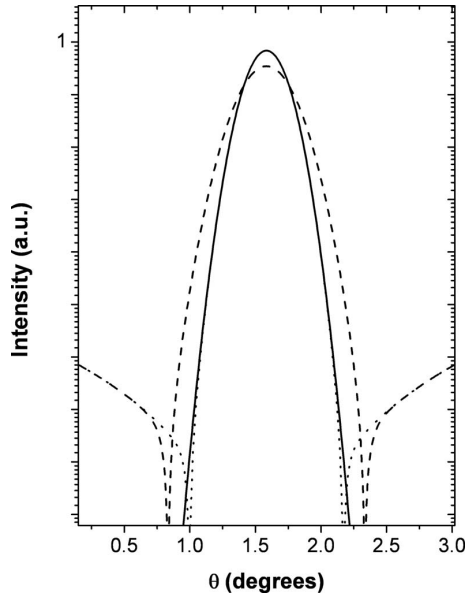

Figure 5
Solid line: Gaussian profile used as reflectivity in the present simulations. Dotted line: Gaussian profile with the scattering owing to the 0.2 nm roughness (r.m.s.). Dashed line: broad diffraction profile curve owing to the random layer thickness fluctuation ($\Delta d/d$) with the scattering owing to the 0.2 nm roughness (r.m.s.).

two mirrors together. If the joint is not perfect, the efficiency of the mirror will be reduced. In our simulations the corner is considered in terms of its size, which is an input parameter in the ray-tracing program. In this region of the mirror, diffraction does not occur, so there is no intensity. This appears as a dark diagonal line in the image after the mirror. In our simulations we consider a corner gap of 2 μm. In this case the intensity loss owing to the corner is 0.2%. However, this value is going to be larger in the center of the mirror (about 60 μm) owing to the pre-figured mirrors. In this case a dark elliptical-shape diagonal is expected in the center of the image after the mirror (schematically shown by arrows in Fig. 6*a*). In our simulations this is not considered; the scripts are being improved to treat this kind of effect. Even in this case, however, the intensity loss owing to the corner is estimated to be less than 2%.

2.7. Statistic fluctuation

Experimental measurements always carry statistic fluctuation. To reproduce it in our model, the Poison statistic (ζ) was introduced in a simple form,

$$\zeta = (I/I_0)^{1/2}, \tag{16}$$

where I/I_0 is the relative intensity in each pixel of the two-dimensional detector that registers the intensity diffracted by the mirror. This is not an input in the ray-tracing program but is processed when the intensities are calculated.

3. Results

The results obtained with the ray-tracing simulations, based on the model previously described in this manuscript, are shown

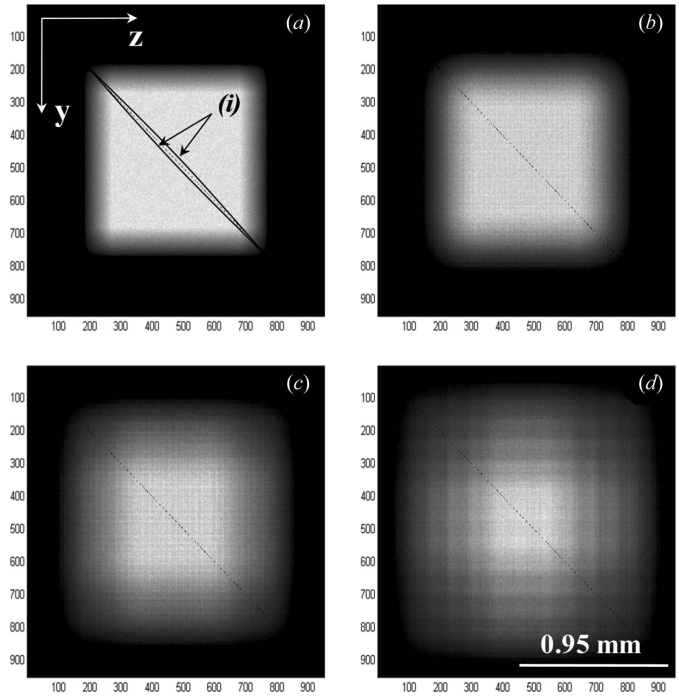

Figure 6
Spot sizes for the parabolic L-shaped laterally graded multilayer mirror. The images were taken at 10 m from the mirror. The pixel size is, approximately, 2 μm × 2 μm. The acceptance is 5 mrad × 5 mrad, the source size is 5 μm × 5 μm and the corner gap is 2 μm. (*a*) Perfect mirror (no slope error; no roughness, $\sigma = 0$; no random variations in the lattice parameter, $\Delta d/d = 0$). (*b*) Slope error 5 μrad, $\sigma = 0.2$ nm, $\Delta d/d = 7 \times 10^{-4}$. (*c*) Slope error 10 μrad, $\sigma = 0.2$ nm, $\Delta d/d = 7 \times 10^{-4}$. (*d*) Slope error 15 μrad, $\sigma = 0.2$ nm, $\Delta d/d = 7 \times 10^{-4}$. The dark diagonal line is the missing intensity owing to the corner gap; (*i*) represents the expected ellipse-like effect induced in the corner owing to the pre-figured surfaces. The area inside the two lines is expected to appear dark. The minor axis of this ellipse, defined by the two lines, is expected to be 60 μm for this mirror.

in Figs. 6–8 for the three different types of L-shaped laterally graded multilayer mirrors: parabolic (Fig. 6), elliptic (Fig. 7) and a combination of both parabolic (vertical mirror for horizontal collimation) and elliptic (horizontal mirror for vertical focusing) (Fig. 8). For the simulations shown here the source size, the acceptance and the mirror corner gap were kept constant with the following values: 5 μm × 5 μm, 5 mrad × 5 mrad and 2 μm, respectively. Also, four different parameter sets were considered for each mirror: (*a*) no slope error, no roughness and no random variations in the lattice parameter ($\Delta d/d$) (perfect mirror); (*b*) slope error of 5 μrad, roughness of 0.2 nm and $\Delta d/d = 7 \times 10^{-4}$; (*c*) slope error of 10 μrad, roughness of 0.2 nm and $\Delta d/d = 7 \times 10^{-4}$; (*d*) slope error of 15 μrad, roughness of 0.2 nm and $\Delta d/d = 7 \times 10^{-4}$.

The spot sizes shown in Figs. 6–8 were taken at 10 m from the mirror. The pixel size on the images is considered to be, approximately, 2 μm × 2 μm. All the images present a blur near the border of the spot; this is due to the source, which contributes for a divergent beam, even for a perfect parabolic mirror. Also, some diffraction effects are clearly shown in some figures. This is mainly due to the defined sinusoidal slope error which induces diffraction effects.

Table 1
Divergence and spot size for different slope errors for the parabolic L-shaped laterally graded multilayer mirror (collimating optics).

Source size (5 μm × 5 μm) and acceptance (5 mrad × 5 mrad) are fixed. Such results were obtained from the ray-tracing simulations shown in Fig. 6.

Slope error (μrad)	Spot size (mm)	Divergence (μrad)
0	1.250 × 1.250	19
5	1.371 × 1.371	37
10	1.571 × 1.571	57
15	1.766 × 1.766	77

Table 2
Divergence and spot size for different slope errors for the elliptic L-shaped laterally graded multilayer mirror (focusing optics).

Source size (5 μm × 5 μm) and acceptance (5 mrad × 5 mrad) are fixed. Such results were obtained from the ray-tracing simulations shown in Fig. 7.

Slope error (μrad)	Spot size (mm)	Divergence (μrad)
0	0.250 × 0.250	84
5	0.387 × 0.387	63
10	0.583 × 0.583	44
15	0.782 × 0.782	19

Quantitative values for the divergence and spot size (FWHM), obtained from these images, are shown in Tables 1, 2 and 3. The diffracted integrated intensity is shown to be constant for all types of mirror, as there were no missed rays owing to the figure errors, because the field of view (1.9 mm × 1.9 mm) is large enough to collect all the rays (for the parameters chosen here). However, the peak intensity can be different. For an ideal mirror the reflectivity shown in Fig. 2 has a peak intensity of 0.85. However, since each ray goes through two diffractions, the peak intensity would be about 0.723 for a perfect L-shaped laterally graded multilayer mirror. This value was confirmed for all three types of mirror. When the figure errors are included, the peak intensity is

Table 3
Divergence and spot size for different slope errors for the elliptic/parabolic L-shaped laterally graded multilayer mirror (vertical focusing and horizontal collimating optics).

Source size (5 μm × 5 μm) and acceptance (5 mrad × 5 mrad). Such results were obtained from the ray-tracing simulations shown in Fig. 8.

Slope error (μrad)	Spot size (mm)	Vertical divergence (μrad)	Horizontal divergence (μrad)
0	1.250 × 0.250	84	19
5	1.371 × 0.387	63	37
10	1.571 × 0.583	44	57
15	1.766 × 0.782	19	77

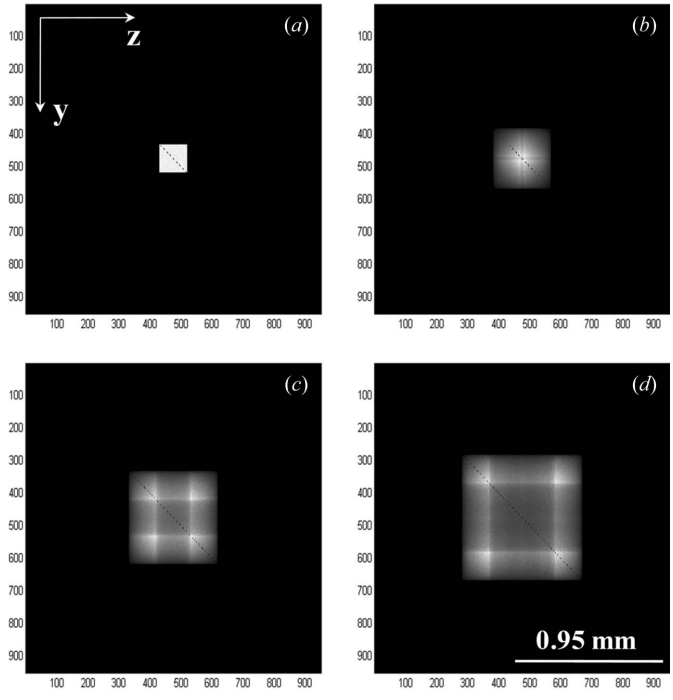

Figure 7
Spot sizes for the elliptic L-shaped laterally graded multilayer mirror. The images were taken at 10 m from the mirror. The pixel size is, approximately, 2 μm × 2 μm. The acceptance is 5 mrad × 5 mrad, the source size is 5 μm × 5 μm and the corner gap is 2 μm. (*a*) Perfect mirror (no slope error; no roughness, $\sigma = 0$; no random variations in the lattice parameter, $\Delta d/d = 0$). (*b*) Slope error 5 μrad, $\sigma = 0.2$ nm, $\Delta d/d = 7 \times 10^{-4}$. (*c*) Slope error 10 μrad, $\sigma = 0.2$ nm, $\Delta d/d = 7 \times 10^{-4}$. (*d*) Slope error 15 μrad, $\sigma = 0.2$ nm, $\Delta d/d = 7 \times 10^{-4}$. The dark diagonal line is the missing intensity owing to the corner gap.

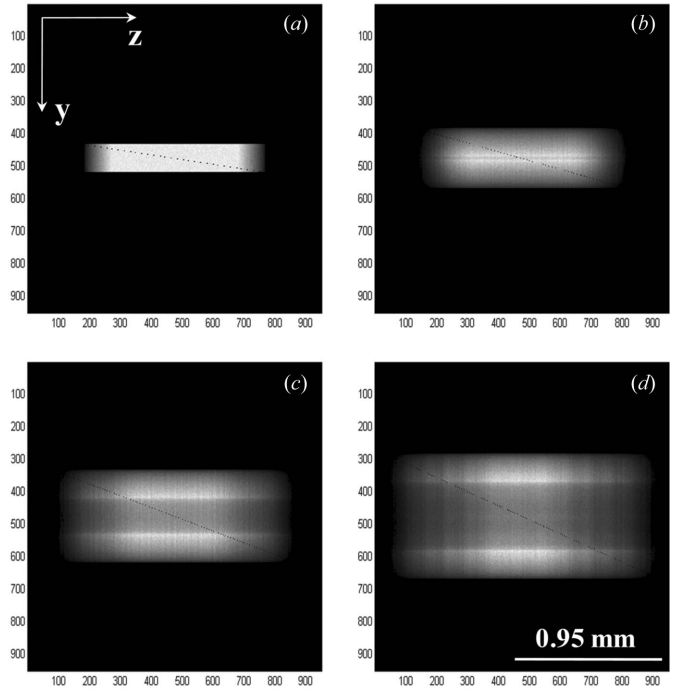

Figure 8
Spot sizes for the elliptic (vertical focusing)/parabolic (horizontal collimation) L-shaped laterally graded multilayer mirror. The images were taken at 10 m from the mirror. The pixel size is, approximately, 2 μm × 2 μm. The acceptance is 5 mrad × 5 mrad, the source size is 5 μm × 5 μm and the corner gap is 2 μm. (*a*) Perfect mirror (no slope error; no roughness, $\sigma = 0$; no random variations in the lattice parameter, $\Delta d/d = 0$). (*b*) Slope error 5 μrad, $\sigma = 0.2$ nm, $\Delta d/d = 7 \times 10^{-4}$. (*c*) Slope error 10 μrad, $\sigma = 0.2$ nm, $\Delta d/d = 7 \times 10^{-4}$. (*d*) Slope error 15 μrad, $\sigma = 0.2$ nm, $\Delta d/d = 7 \times 10^{-4}$. The dark diagonal line is the missing intensity owing to the corner gap.

reduced. The main reason for this is the loss of intensity owing to the roughness (σ) and owing to the random variations in the lattice parameter ($\Delta d/d$), especially for the parabolic mirror. For the elliptic and elliptic/parabolic mirror another contribution for the loss of peak intensity is the slope error. For this reason the peak intensity value changes for the different figure error parameters. The slope error can also affect the peak intensity for a parabolic mirror but only for large values (above 20 µrad).

The divergence is strongly dependent on the source size and on the slope error. If the source size is kept constant at 5 µm × 5 µm (constant for all simulations), the changes in the divergence are caused by the angular spread of the beam owing to the slope error. For a perfect figure, the parabolic mirror showed a divergence of 19 µrad × 19 µrad; this is due to the source. When the slope error is included, the divergence (Table 1) and the spot size (Fig. 6) are increased. On the other hand, for a perfect figure, the elliptic mirror showed a divergence of 84 µrad × 84 µrad; this is also due to the source. When the slope error is included, the divergence (Table 2) is decreased while the spot size is increased (Fig. 7). This can be understandable because a perfect focusing mirror does not have aberrations (convergent mirror) and, when some figure errors are included, this mirror is no longer a perfect convergent mirror and starts to deliver a less convergent beam. For the elliptic/parabolic mirror (vertical focusing/horizontal collimating) the results are a combination of elliptic and parabolic mirror, as shown in Table 3. Another important parameter is how perpendicular the L-shape arrangement is. By using a geometric approach shown elsewhere (Beaumont & Hart, 1974), we estimated the required value for the tolerance in the perpendicularity. We found that such a parameter can be off by an angle of 50 µrad, in order to keep the values shown in Tables 1–3 within the range of 5%.

The optimized slope-error parameter for the L-shaped laterally graded multilayer mirror for the IXS beamline at NSLS II was selected to be 10 µrad, because the integrated intensity is the same for 5 µrad as for 15 µrad, the spot size (Fig. 8) is about 0.5 mm × 1.2 mm (for the elliptic/parabolic mirror) and the divergence is 44 µrad (vertically) × 57 µrad (horizontally). These parameters are considered small enough for our requirements.

For comparison purposes, a ray tracing for the parabolic L-shaped multilayer mirror (non-laterally graded) obtained using *SHADOW* is shown in Fig. 9. *SHADOW* is not able to handle the laterally graded multilayer mirror; however, the results for the divergence are compatible with the results obtained with the ray-tracing scripts described within this manuscript.

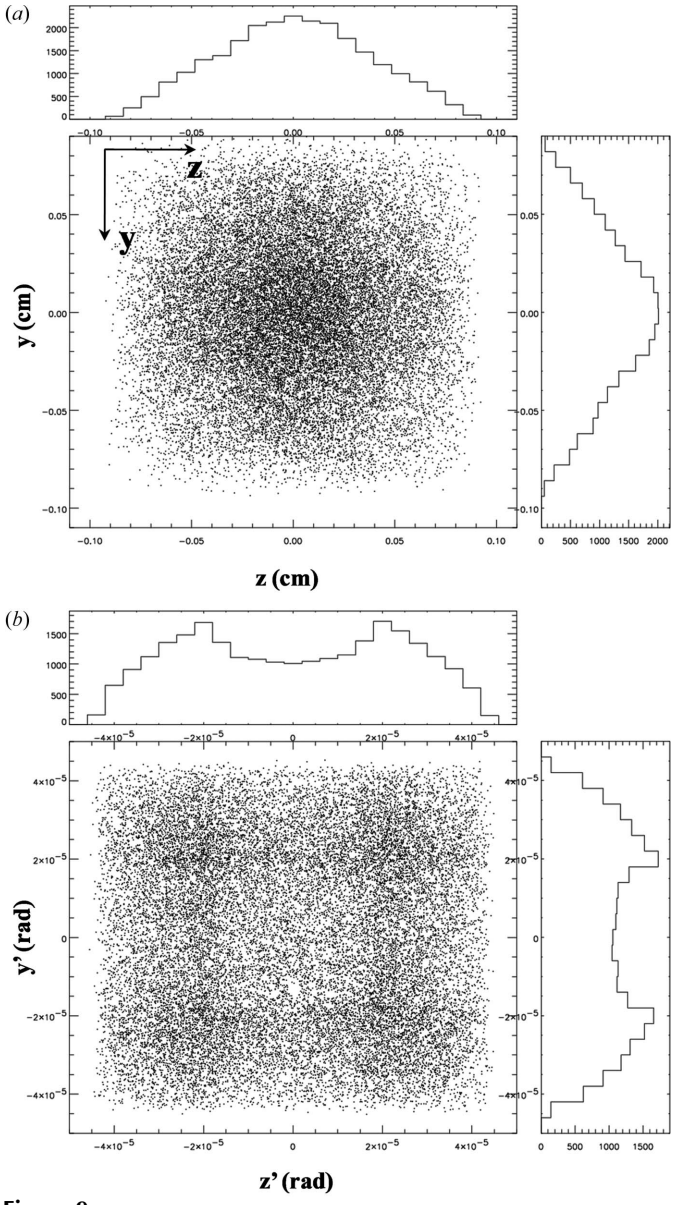

Figure 9
(*a*) Spot size for the parabolic L-shaped multilayer mirror (non-laterally graded) obtained using the software *SHADOW*. The images were taken at 10 m from the mirror. The acceptance is 5 mrad × 5 mrad, the source size is 5 µm × 5 µm. Slope error 10 µrad, $\sigma = 0.2$ nm, $\Delta d/d = 7 \times 10^{-4}$. (*b*) Divergence plot (y' *versus* z') for the former parameters. Total number of rays: 25000.

4. Conclusion

A theoretical model to trace X-rays through an L-shaped laterally graded multilayer mirror has been presented here. The model included different types of surfaces, multilayer types/thickness and several other parameters (such as roughness, slope error, random variation in the lattice parameter, corner effects *etc.*). Three types of L-shaped mirrors were traced: collimator (parabolic figure), focusing optics (elliptic figure) and focusing/collimator optics (combining elliptic and parabolic figure). The results show that the theoretical model was able to confirm the expected spot sizes and divergences. An extended option based on challenging surfaces such as asphericals with polynomial curvatures (parabolic paraboloid and parabolic ellipsoid) is being implemented. Also, these ray-tracing scripts were useful for estimating the specification requirements based on our performance needs [slope error (r.m.s.) 10 µrad, roughness (r.m.s.) 0.2 nm, $\Delta d/d = 7 \times 10^{-4}$ and corner gap 2 µm] and to confirm that such optics could

also be used for synchrotron applications as an alternative to the Kirkpatrick–Baez geometry or to a single aspheric-type mirror.

This work was supported by the US Department of Energy, Office of Science, Office of Basic Energy Sciences, under contract No. DE-AC-02-98CH10886.

References

Authier, A. (2001). *Dynamical Theory of X-ray Diffraction.* Oxford University Press.

Beaumont, J. H. & Hart, M. (1974). *J. Phys. E*, **7**, 823–829.

Bruson, A. (1995). *J. Appl. Phys.* **77**, 1001–1009.

Champeaux, J.-Ph., Troussel, Ph., Villier, B., Vidal, V., Khachroum, T., Vidal, B. & Krumrey, M. (2007). *Nucl. Instrum. Methods Phys. Res. A*, **581**, 687–694.

Debye, P., Anderson, H. R. Jr & Brumberger, H. (1957). *J. Appl. Phys.* **28**, 679–683.

Dumond, J. & Youtz, J. P. (1940). *J. Appl. Phys.* **11**, 357–365.

Hertlein, F., Oehr, A., Hoffmann, C., Michaelsen, C. & Wiesmann, J. (2005). *Part. Part. Syst. Charact.* **22**, 378–383.

Honnicke, M. G. & Cusatis, C. (2009). *J. Appl. Cryst.* **42**, 999–1003.

Ice, G. E., Pang, J. W. L., Tulk, C., Molaison, J., Choi, J.-Y., Vaughn, C., Lytle, L., Takacs, P. Z., Andersen, K. H., Bigault, T. & Khounsary, A. (2009). *J. Appl. Cryst.* **42**, 1004–1008.

Jain, V. K. (2008). *Machin. Sci. Technol.* **12**, 257–294.

Kirkpatrick, P. & Baez, A. V. (1948). *J. Opt. Soc. Am.* **38**, 766–774.

Kopecky, M. (1994). *J. Appl. Phys.* **77**, 2380–2387.

Kordonski, W. & Jacobs, S. D. (1996). *Int. J. Mod. Phys. B*, **10**, 2837–2848.

Lai, B. & Cerrina, F. (1986). *Nucl. Instrum. Methods Phys. Res. A*, **246**, 337–341.

Lienert, U., Poulsen, H. F., Honkimäki, V., Schulze, C. & Hignette, O. (1999). *J. Synchrotron Rad.* **6**, 979–984.

Parrat, L. G. (1954). *Phys. Rev.* **95**, 359–369.

Rhoades, L. (1991). *J. Mater. Proc. Technol.* **28**, 107–116.

Sanchez del Rio, M. & Marcelli, A. (1992). *Nucl. Instrum. Methods Phys. Res. A*, **312**, 170–177.

Schafers, F. (2008). *Modern Development in X-ray and Neutron Optics, Springer Series on Optical Sciences*, Vol. 137, edited by A. Erko, M. Idir, Th. Krist and A. G. Michette. Berlin: Springer.

Schuster, M. & Gobel, H. (1995). *J. Phys. D*, **28**, A270–A275.

Shymanovich, U., Nicoul, M., Sokolowski-Tinten, K., Tarasevitch, A., Michaelsen, C. & Von der Linde, D. (2008). *Appl. Phys. B*, **92**, 493–499.

Shvyd'ko, Yu. V., Lerche, M., Kuetgens, U., Ruter, H. D., Alatas, A. & Zhao, J. (2006). *Phys. Rev. Lett.* **97**, 235502.

Sinha, S. K., Sirota, E. B., Garoff, S. & Stanley, H. (1988). *Phys. Rev. B*, **38**, 2297–2311.

Stepanov, S. A., Kondrashkina, E. A., Schmidbauer, M., Kohler, R. & Pfeifer, J.-U. (1996). *Phys. Rev. B*, **54**, 8150–8162.

Sugisaki, K., Takahashi, S., Yoshidomi, Y., Shinada, K., Mitomi, O., Uchishiba, E., Hamada, R., Kato, T. & Aoki, S. (1998). *Appl. Opt.* **37**, 8057–8066.

Toellner, T. S., Hu, M. Y., Sturhahn, W., Quast, K. & Alp, E. E. (1997). *Appl. Phys. Lett.* **71**, 2112–2114.

Underwood, J. H. & Barbee, T. W. Jr (1981). *Appl. Opt.* **20**, 3027–3034.

Vainer, Yu. A., Pestov, A. E., Prokhorov, K. A., Salashchenko, N. N., Fraerman, A. A., Chernov, V. V. & Chkhalo, N. I. (2006). *J. Exp. Theor. Phys.* **103**, 346–353.

Vinogradov, A. V. & Zeldovich, B. Ya. (1977). *Appl. Opt.* **16**, 89–93.

Wong, Po-z. (1985). *Phys. Rev. B*, **32**, 7417–7424.

Yabashi, M., Tamasaku, K., Kikuta, S. & Ishikawa, T. (2001). *Rev. Sci. Instrum.* **72**, 4080–4083.